Strain and stress relation for non-linear finite element simulations

Sören Ehlers *, Petri Varsta

Helsinki University of Technology, Marine Technology, PL 5300, 02015 TKK, Finland

ARTICLE INFO

ABSTRACT

This paper presents a procedure to determine an element-length dependent strain and stress relation until fracture that is suitable for implementation in finite element models. This material relation is obtained experimentally with an optical measuring system. The strain until fracture is calculated from the measured surface displacements. The stress is derived from the measured force and the cross-sectional area in the necking region. Furthermore, because of the digital nature of the optical measurements, the strain reference length, being a function of the pixel size, is clearly defined. For the numerical simulation the finite element length is equal to this strain reference length. The overall procedure allows a precise numerical simulation of the tensile experiment until the point of fracture without curve fitting or an iterative procedure to adjust the material relation for the chosen mesh size. This precise material relation can improve non-linear numerical simulations.

© 2009 Elsevier Ltd. All rights reserved.

1. Introduction

Non-linear finite element simulations, such as crashworthiness analysis, require the input of the true strain and stress relation until failure. Failure is especially crucial in ship-related simulations where the leakage is of interest. The true strain should be obtained by using an infinitesimally small gauge length to capture the strain localisation in the necking region. Additionally, the finite element method requires a discrete model, i.e. a meshed model, and therefore the finite element length has to correspond to this small gauge length, i.e. the strain reference length. The true stress should be obtained independently of the strain as a function of the cross-sectional area at any given instant.

The stress and strain relation from standard tensile experiments is used for finite element simulations by Joun et al. [1], Koc and Stok [2], Mirone [3], Paik [4], and Springmann and Kuna [5]. However, it remains in question if the chosen finite element length corresponds to the strain reference length. For one selected finite element length, agreement between the numerical simulation and the experiment may be achieved by an iterative procedure. Here the true strain and stress relation used as input for the simulation is changed until compliance with the corresponding experiment is achieved (Huatao and Roehr [6], Isselin et al. [7], Zhang [8], and Zhang et al. [9]). Bridgman's [10] empirical correction factors for the post-necking region were used by Ling [11] to determine the true strain and stress for tensile experiments on copper alloys in an iterative finite element-based

procedure. However, Ling does not define the strain reference length.

To obtain the true strain and stress for a tensile specimen, Hoffmann and Vogl [12] used optical measurements. Neither they do not validate their measured material relation with the corresponding tensile test results, and nor do they define the strain reference length.

Of the papers mentioned, only Springmann and Kuna [5] contribute to the prediction of failure, i.e. to the end point of the true stress and strain curve, by means of a damage parameter based on fracture mechanics. The true strain and stress until failure are traced by Hoffmann and Vogl [12], Huatao and Roehr [6], Joun et al. [1], Koc and Stok [2], Ling [11], Mirone [3], and Paik [4], but no prediction of the failure strain is presented.

Therefore, the aim of this paper is to obtain experimentally a true strain and stress relation until failure that is suitable for implementation in finite element models and to define the strain reference length. The strain and stress relation is obtained with an optical measuring system, which measures the local displacements at the surface of the specimen. From these displacement values the local strain is calculated on the basis of a discrete amount of pixel recordings, a so-called facet. The discrete pixel dimension will clearly define the strain reference length. One pixel records $29.3 \times 29.3\,\mu m^2$ of the specimen's surface area for the experiments presented herein. To determine the true stress, the cross-sectional area at any given instant is calculated on the basis of the out-of-plane displacement measurements of the specimen. The overall experimental figures are given in Ehlers and Enquist [13].

This non-iterative determination of the true strain and stress relation is used as input for the finite element simulations, where the finite element length is equal to the strain reference length.

* Corresponding author. Tel.: +358 9 451 3497; fax: +358 9 451 4173.
E-mail addresses: soeren.ehlers@tkk.fi, soeren.ehlers@gmail.com (S. Ehlers).

The measured local failure strain serves as a criterion to delete elements to simulate rupture or to terminate the simulation at the point of rupture. A finite element simulation of the tensile experiment validates the proposed procedure to obtain a strain and stress relation. The numerical result is compared to the force and elongation recorded independently of the optical measurements.

2. Tensile specimens

The dog-bone specimens, with different length-per-breadth ratios (L/B), consist of 4-mm-thick NVA and 6-mm-thick RAEX S275 LASER steels; see Table 1 and Fig. 1. The specimens are water-cut with their longitudinal direction parallel to the rolling direction of the plates. Details of the production of the specimens are given in Ehlers and Enquist [13] and the chemical composition of the material is given in Remes [14].

3. Tensile experiments

3.1. Test set-up

The three tensile specimen types were tested with three specimens each. The displacement-controlled experiments are carried out with a tensile test machine at Växjö University, consisting of a MTS 322 Test Frame with Load Unit. The MTS Test Frame records the force and the resulting elongation of the specimens, in other words the force-elongation curve, which will be used to validate the proposed procedure.

3.2. Optical measurements

The optical measuring system is positioned on a tripod independent of the MTS Test Frame. ARAMIS 4 M, produced by Gesellschaft für Optische Messtechnik, is used for the experiments presented here. A stochastic pattern needs to be placed onto the specimen's surface in order for the optical measuring system to be
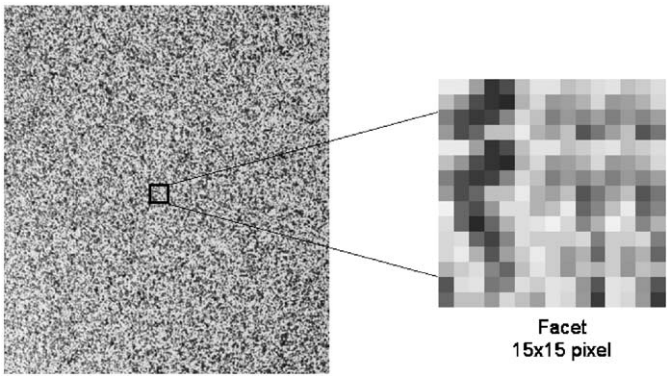

Fig. 2. Stochastic pattern of the surface of the specimen with a facet of 15×15 pixels.
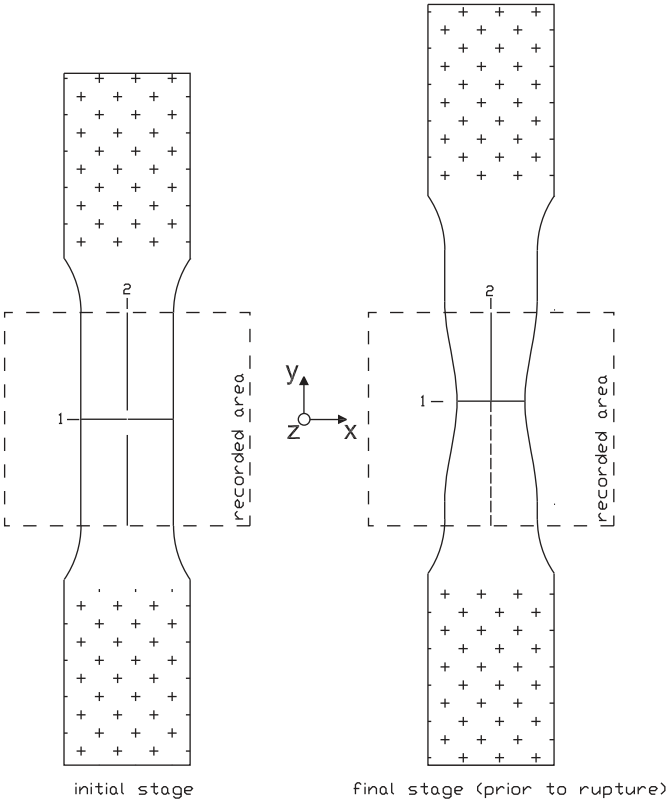
Fig. 3. Location of the sections on the surface of the specimen.

Table 1
Tensile specimen dimensions in mm.

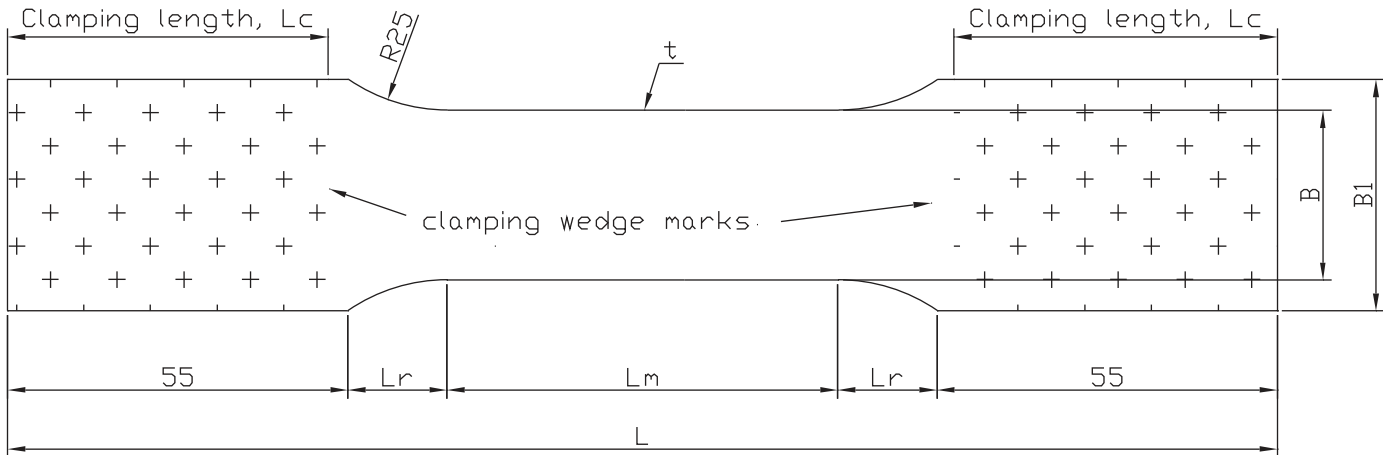| ~L/B	L	B	B2	Lc	Lr	Lm	Thickness
8	194.1	24.22	33	48.54	13.8	56.5	4.04
8.5	206.8	24.34	33	50.06	13.8	69.2	5.87
11.6	250	21.54	29	48.58	12	116	5.90

Fig. 1. Principal dimensions of dog-bone type tensile specimen.

used. The pattern is obtained by applying a matt white-base spray paint layer followed by a sprinkling of matt black spray paint; see Fig. 2.

Two 4-megapixel cameras record synchronised stereo images of the specimen with a delay time between consecutive images of 6 s. Therefore, the measuring point density is 0.2 mm of the applied displacement speed of 2 mm/min. The recorded images of the stochastic pattern consist of grouped pixels, so-called facets. Fig. 2 shows a 15×15 pixels facet as an example. Each facet contains individual greyscale information and can, therefore, be traced throughout the experiment. To assess the sensitivity of the facet size on the results, a selection of seven facet sizes is made ranging from 10×10 to 50×50 pixels. The 10×10 pixels facet is the smallest traceable facet, whereas the 50×50 pixels facet is still sufficiently small to capture local effects for the specimens tested.

From the full 3D measurement point recordings, in other words the facet recordings, the selection of sections can be made. Fig. 3 shows the recorded area and the selected section locations on the specimen's surface for the initial stage and for the final stage of deformation prior to surface fracture. Section 1 is located at the minimum cross-section of the neck and Section 2 intersects Section 1 at the point of maximum strain prior to failure. For each section the 3D coordinates, displacements, and strains, i.e. the strain localisation, are determined on the surface of the specimen in each loading stage; see Fig. 4. A coordinate transformation of the recorded loading stages compensates for rigid body movements; see Appendix A. This transformation relates the 3D coordinates of the deformed stages to a reference plane fit through the undeformed specimen surface.

3.3. Strain determination

The strains are determined on the basis of facets on the surface of the specimen, in other words, local strains, which are tangential to the surface. The strain is calculated from the measured and linearly interpolated elongation of a line element, i.e. strain reference length, connecting 3-measured 3D points, i.e. facets. With the selected facet sizes in pixels and with a facet overlap of 10–13 percent, the distance between each measured 3D point, respectively the strain reference length, is given in Table 2. These

facet sizes are used for all three types of specimen. Hence, the true strain ε_T can be defined in 1D by

$$\varepsilon_T = \ln\left(\frac{l + \delta l}{l}\right), \tag{1}$$

where l is strain reference length and δl is the change in the length of l for consecutive stages. The extension of this 1D case to 3D can be found in the Appendix A of this paper.

Fig. 4 shows the longitudinal strain distribution of Section 2 as an example for a facet size of 15×15 pixels. The strain localisation, in other words the necking phenomena, is depicted by the sharp strain peak. The strain reference length determines the maximum strain-peak value to be captured. Fig. 5 presents the strain localisation for each specimen. The true strain in the neck is plotted versus the engineering strain until the onset of surface fracture, i.e. until failure strain. It can be seen that the curves become steeper with growing L/B ratios and at the same time varying the specimen thickness. The global strain calculated from the elongation measurements with reference to the effective length Lm of the specimen (see Fig. 1) is represented by the solid line according to $\varepsilon_T = \ln(1+\varepsilon_E)$. Hence a significant difference in numerical values exists between the locally and globally measured strains. This difference justifies the localised measurements with respect to finite element simulations, where the required strain data need to be element length dependent. This element-length dependency is now obtained, as the finite element length has to be equal to the strain reference length, see Table 2. This allows the simulation of the onset of fracture at the correct strain. The measured failure strain values are given in Table 3 and plotted versus the facet size in Fig. 6. The constant

Table 2
Facet size in *pixels* and strain reference length in mm.

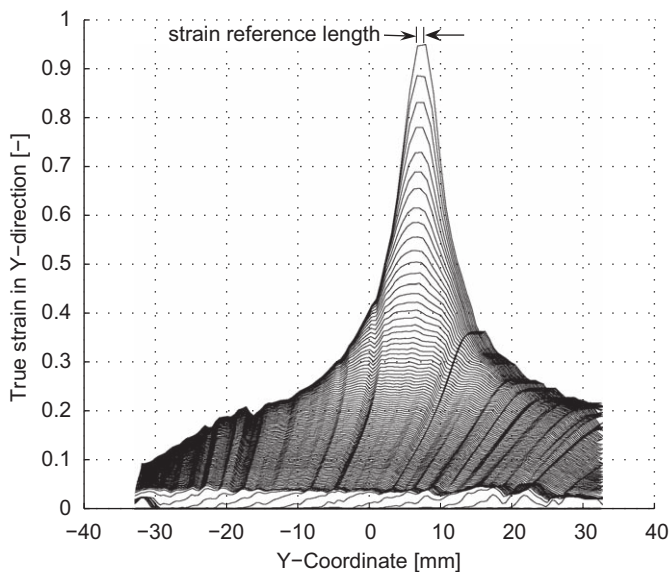| Facet size	Strain reference length
10×10	0.88
15×15	1.32
20×20	1.76
25×25	2.2
30×30	2.64
40×40	3.52
50×50	4.4

Fig. 4. Measured true strain in *Y*-direction versus *Y*-coordinate for each captured stage for Section 2 (facet size 15×15 pixels, $L/B = 8$).
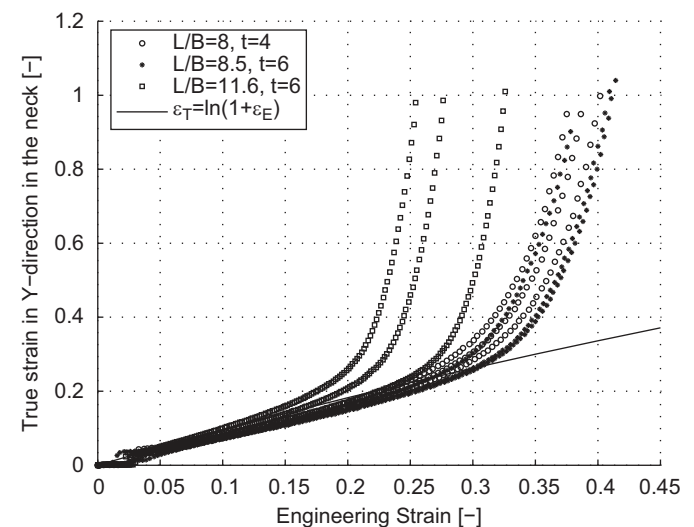

Fig. 5. Measured true strain in the neck versus engineering strain (facet size 15×15 pixels).

Table 3
Measured strain, strain triaxiality, Lode angle and parameter at the point of failure (average values for each L/B ratio).

~L/B	Facet size	Failure strain	Strain triaxiality	Lode angle (deg.)	Lode parameter
8	10 × 10	1.018	0.016	37.714	−0.257
	15 × 15	0.965	0.085	31.116	−0.037
	20 × 20	0.954	0.038	35.488	−0.183
	25 × 25	0.891	0.042	34.720	−0.157
	30 × 30	0.871	0.046	34.231	−0.141
	40 × 40	0.772	0.055	32.193	−0.073
	50 × 50	0.692	0.034	33.133	−0.104
8.5	10 × 10	1.081	0.062	34.274	−0.142
	15 × 15	1.020	0.082	31.073	−0.036
	20 × 20	0.989	0.074	32.053	−0.068
	25 × 25	0.946	0.071	32.242	−0.075
	30 × 30	0.883	0.071	31.863	−0.062
	40 × 40	0.820	0.067	31.095	−0.037
	50 × 50	0.742	0.055	31.437	−0.048
11.6	10 × 10	1.044	0.080	31.555	−0.052
	15 × 15	0.992	0.074	31.340	−0.045
	20 × 20	0.944	0.067	31.208	−0.040
	25 × 25	0.911	0.065	31.310	−0.044
	30 × 30	0.869	0.058	31.958	−0.065
	40 × 40	0.804	0.054	32.147	−0.072
	50 × 50	0.702	0.047	31.647	−0.055

3.4. Stress determination

Unlike the local strain determination, the stress cannot be measured at the strain reference length. Therefore the local stress is determined on the basis of the minimum cross-sectional area of the specimen measured as a function of the facet size. In other words the cross-sectional area becomes larger with increasing facet sizes, as the localization is averaged over the extent of the facet size, see Fig. 7. The normal stress distribution at the cross-section of the specimen becomes constant as soon as the cross-section is subjected entirely to plastic flow, since no shear stresses occur. Hence, the force elongating the specimen and the cross-section at any given instant of the specimen define the average local stress on a cross-section of the specimen by

$$\sigma_T = \frac{F}{A}. \tag{2}$$

The cross-section at any given instant is calculated on the basis of the out-of-plane displacement of Section 1; see Fig. 8 as an

Fig. 7. Measured relative cross-sectional area versus true strain in Y-direction as a function of the chosen facet sizes.
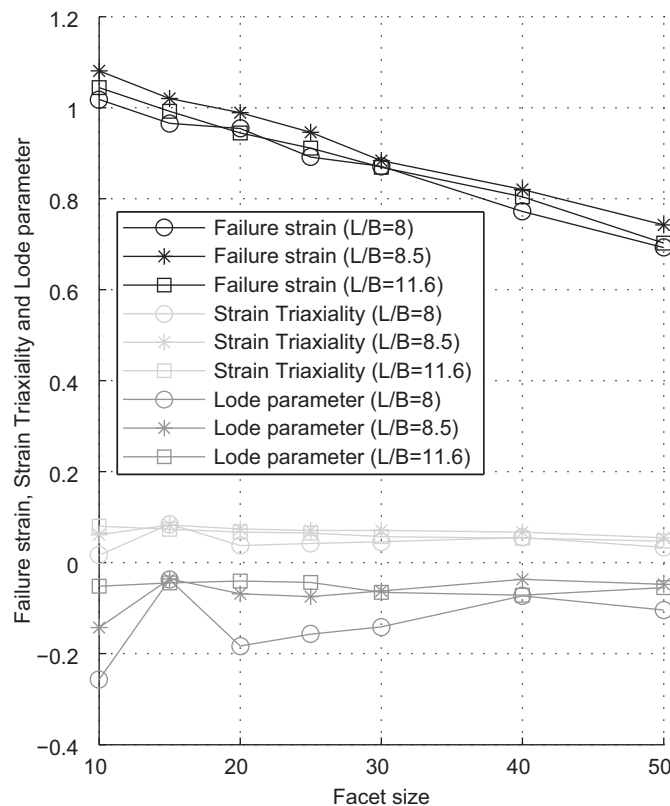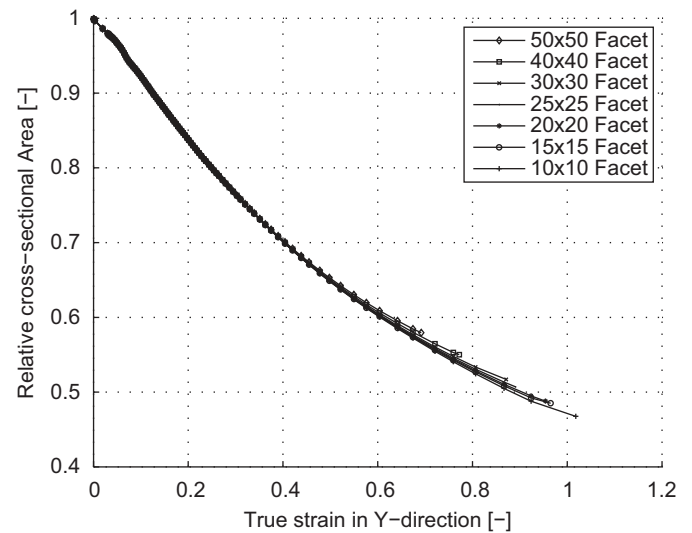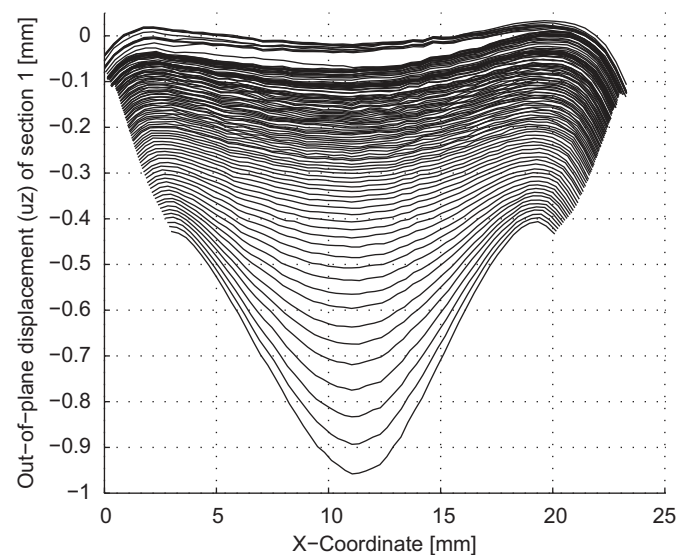

Fig. 6. Failure strain, strain triaxiality and Lode parameter as a function of the chosen facet sizes.

strain failure criteria is chosen as close ranges of strain triaxiality, Lode angle and parameter are attained at the failure initiation points, see Table 3 and Fig. 6. The histories of the strain triaxiality, Lode angle and parameter versus the true strain in Y-direction are given in Appendix B. Except for some slight deviations in Lode angle and parameter of the L/B = 8 specimens, all histories are in very close range.

Fig. 8. Measured out-of-plane displacement for each captured stage for Section 1 (L/B = 8).

example for a facet size of 15×15 pixels. The breath reduction of the specimen is obtained from the X-coordinate values. Therefore, the cross-sectional area of the specimen at any given instant can be calculated on the basis of these out-of-plane displacement data, measured on one specimen surface and assuming symmetrical cross-sectional change for each stage until failure according to

$$A(y) = \int [t + 2\,u_z(x,y)]\,dx, \tag{3}$$

where y indicates the position of Section 1 given in Fig. 3, t the initial thickness of the specimen given in Table 1, and u_z the measured out-of-plane displacement given for each stage as an example in Fig. 8. A macro sample study of the cross-sections of the broken specimen justifies the assumption of symmetrical cross-sectional change; see Fig. 9. Additionally, the uppermost line, the initial stage, in Fig. 8 depicts the level of the surface flatness of the specimen and shows the slightly rounded specimen edges; see also Fig. 9. Both the surface flatness and the rounded edges are a result of the production of the specimen.

The resulting relative cross-sectional area versus the measured true strain in the neck in the Y-direction until the onset of fracture for all experiments is given in Fig. 10. The deviation from the constant volume assumption, where $\varepsilon = \ln(A_0/A)$, at larger strains necessitates the out-of-plane displacement measurements to determine the cross-sectional area A at any given instant.

3.5. Strain and stress relation

The average true strain and stress relation obtained from the optical measurements is plotted until the onset of fracture in Figs. 11–13. The average relation of the three specimens tested for each L/B ratio is chosen to clearly present the differences in true
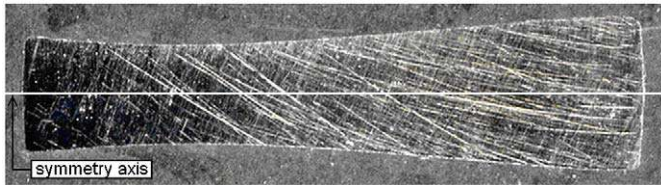

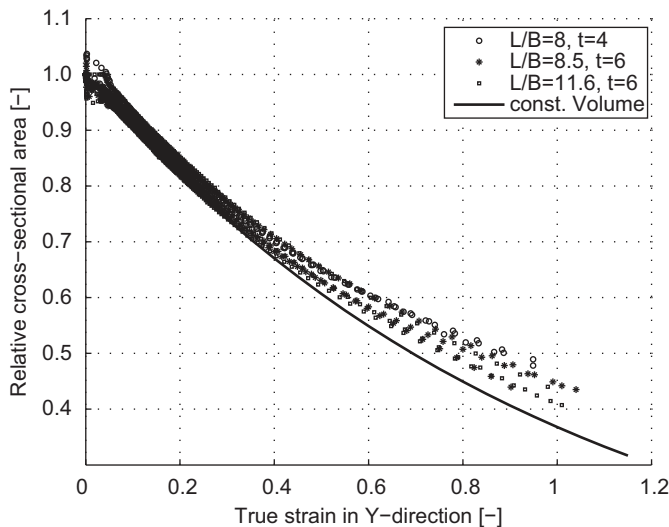**Fig. 9.** Macro sample of the cross-section of the specimen.

Fig. 10. Measured relative cross-sectional area versus measured true strain in the neck.

stress versus strain for the selected facet sizes. The decreasing stress and failure strain is in very good correspondence with the increase in facet size. This averaged and facet-size dependent strain and stress relation is used as input for the finite element simulation.

The measured engineering stress versus strain data from the MTS Test Frame and the corresponding averaged logarithmic stress versus strain, where $\varepsilon_T = \ln(1+\varepsilon_E)$ and $\sigma_T = \sigma_E(1+\varepsilon_E)$, is plotted therein for comparison. Some scatter in engineering stress versus strain curves that exists due to differences in actual specimen geometry and probable material defects within the specimen. The total error arising from the experimental set-up is estimated to be less than 2% and, therefore, only influences the presented procedure nominally; details are given in Ehlers and Enquist [13].

4. Finite element implementation

This chapter utilises the material data determined by the optical measurements presented in Figs. 11–13 with the averaged failure strain from Table 3 to simulate the experiment with the finite element method.

The tensile experiments are simulated using the explicit time integration solver LS-DYNA version 971. The choice of the explicit solver arises from the fact that the proposed strain and stress relation should be applicable for crash analysis of thin-walled structures, see Liu [15] and Zarei and Kröger [16], and ship collision analysis, see Ehlers et al. [17]. For crash analysis involving contact and large shell deformations, the explicit solver proved to be a robust choice, whereas the implicit solver may not converge with increasing non-linearities, see Harewood and McHugh [18]. The structures are modelled using four nodded quadrilateral Belytschko–Lin–Tsay shell elements. This one point quadrature shell element uses discrete Mindlin shell theory to describe displacements and rotations.

The finite element length is equal to the strain reference length. Due to different specimen geometries a deviation in actual element length of up to 2% may exist for some of the meshed models. The specimen is modelled between the clamping wedges only, and therefore the total length of the model is $L_{FEM} = L - 2Lc$. The translational degrees of freedom are prohibited at one edge, whereas the other edge is subjected to a constant displacement of $100 \times$ the experimental speed as no dynamic effects occur. Additionally, the simulation time remains desirably short. The averaged experimentally determined strain and stress relations are implemented via Material 124 of LS-DYNA. Standard LS-DYNA hourglass and time step control is used. For details of the modelling and simulation processes see Ehlers et al. [17,19], Hallquist [20], and Tabri et al. [21]. The initiation and propagation of fracture in the specimens is modelled in LS-DYNA by deleting the failing elements from the model. The element fails once the failure strain is reached.

The resulting force-elongation curves of the finite element simulations are shown in Figs. 14–16. The finite element simulation using the strain reference length dependent and averaged strain and stress relation presented in Figs. 11–13 complies with very good agreement to the independently measured average MTS recordings. The point of failure, in other words the end of the curves, is captured accurately by the numerical simulation, especially for element lengths up to 2.2 mm.

For reference and comparison the same finite element models are used with an average power material law fit ($K = 760$, $n = 0.23$, $\varepsilon_f = 0.86$ for $L/B = 8$, $K = 745$, $n = 0.22$, $\varepsilon_f = 0.92$ for $L/B = 8.5$ and $K = 755$, $n = 0.23$, $\varepsilon_f = 0.93$ for $L/B = 11.6$) according
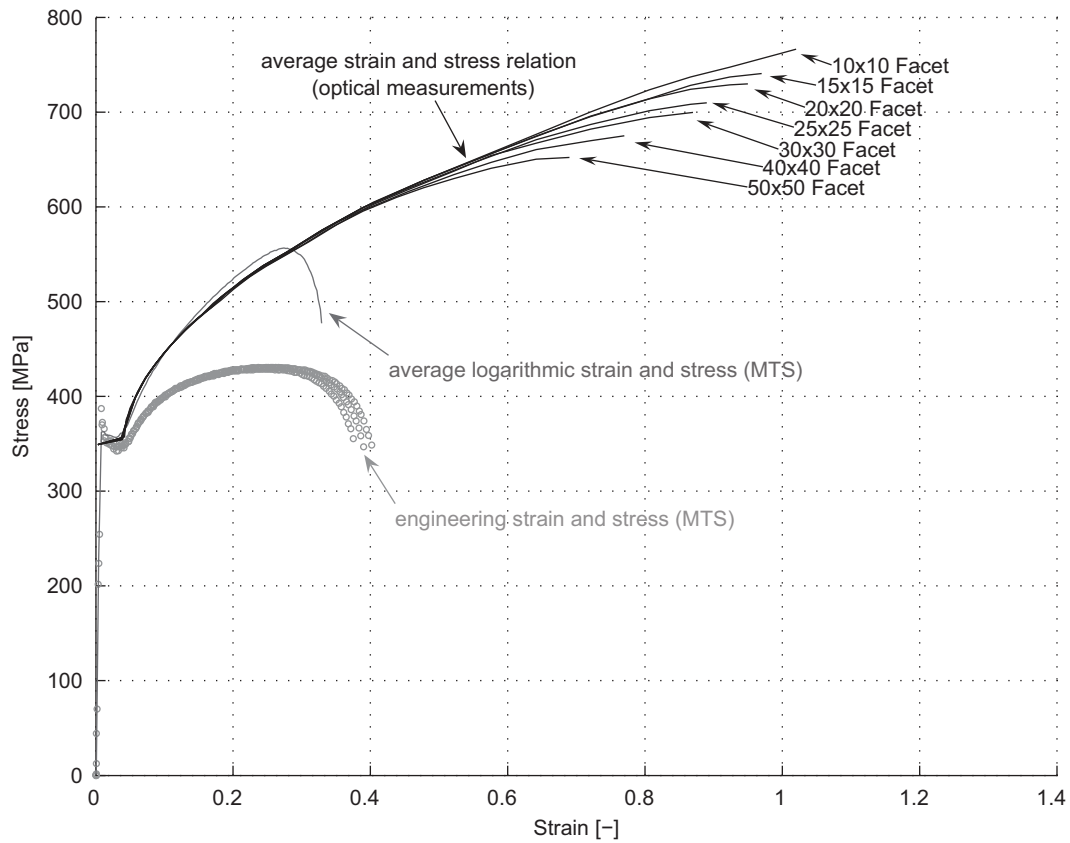
Fig. 11. Measured strain and stress relation ($L/B = 8$, MTS measures are plotted for comparison).
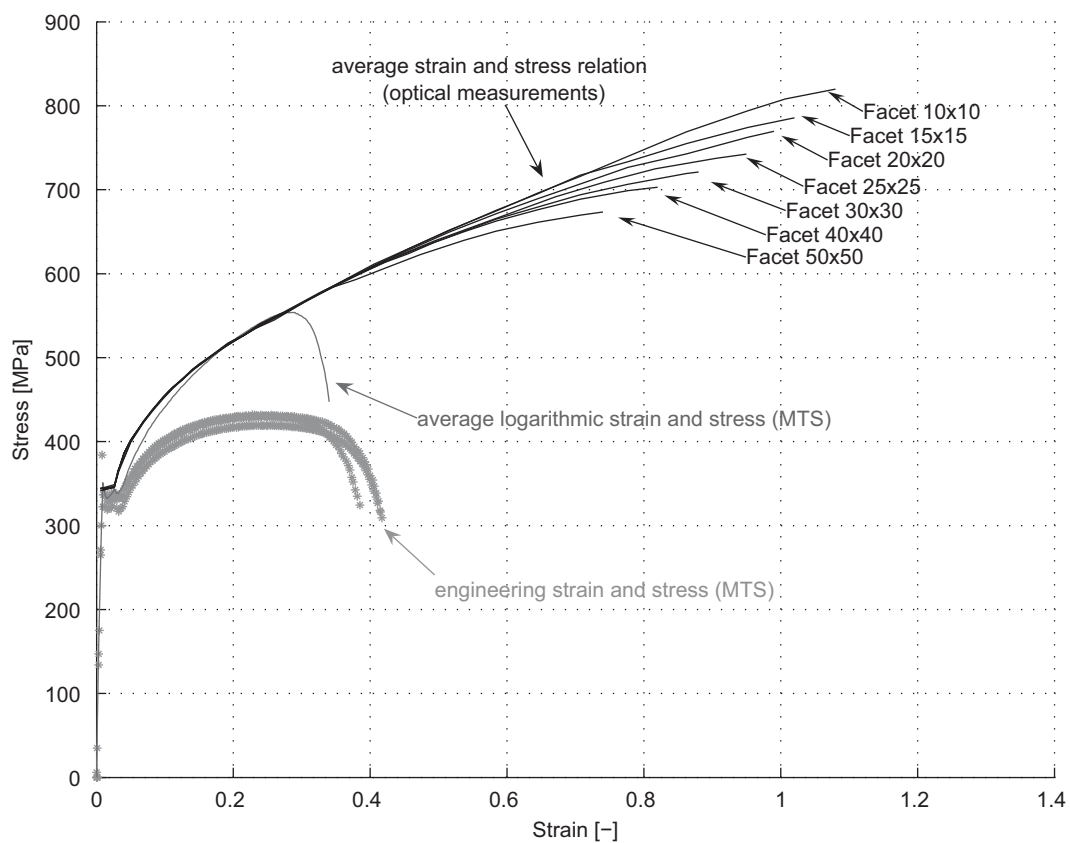

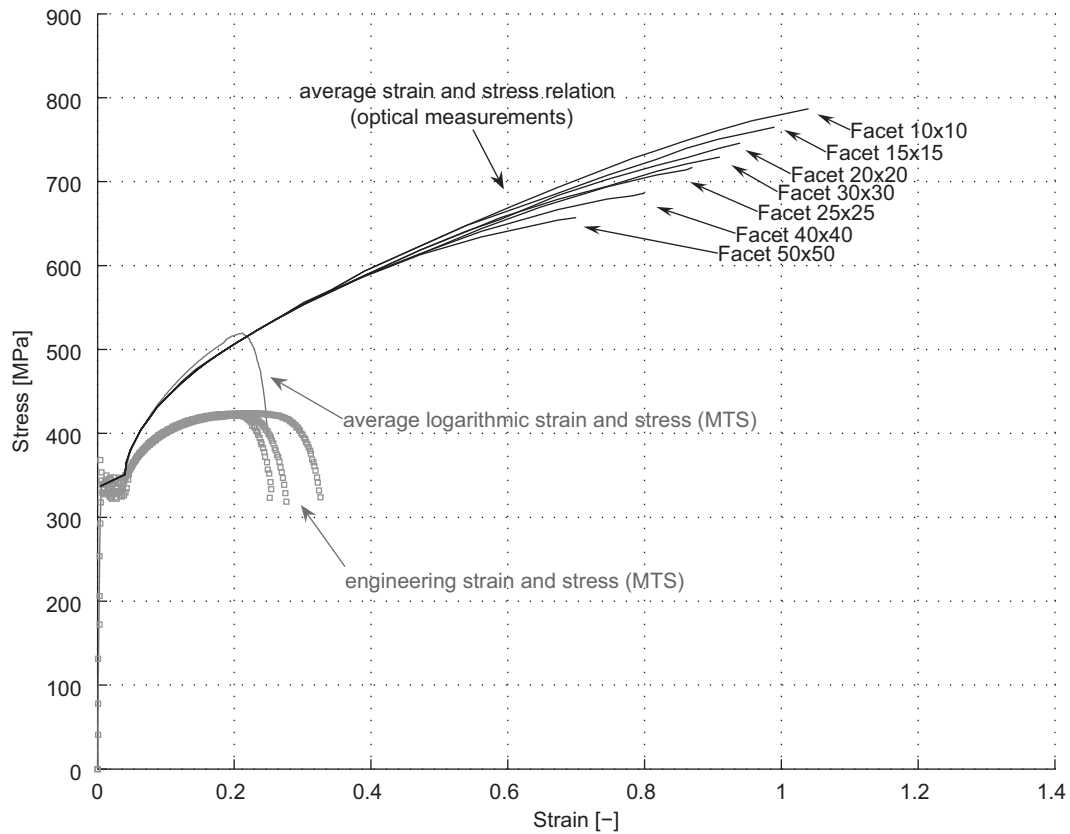**Fig. 12.** Measured strain and stress relation ($L/B = 8.5$, MTS measures are plotted for comparison).

Fig. 13. Measured strain and stress relation ($L/B = 11.6$, MTS measures are plotted for comparison).
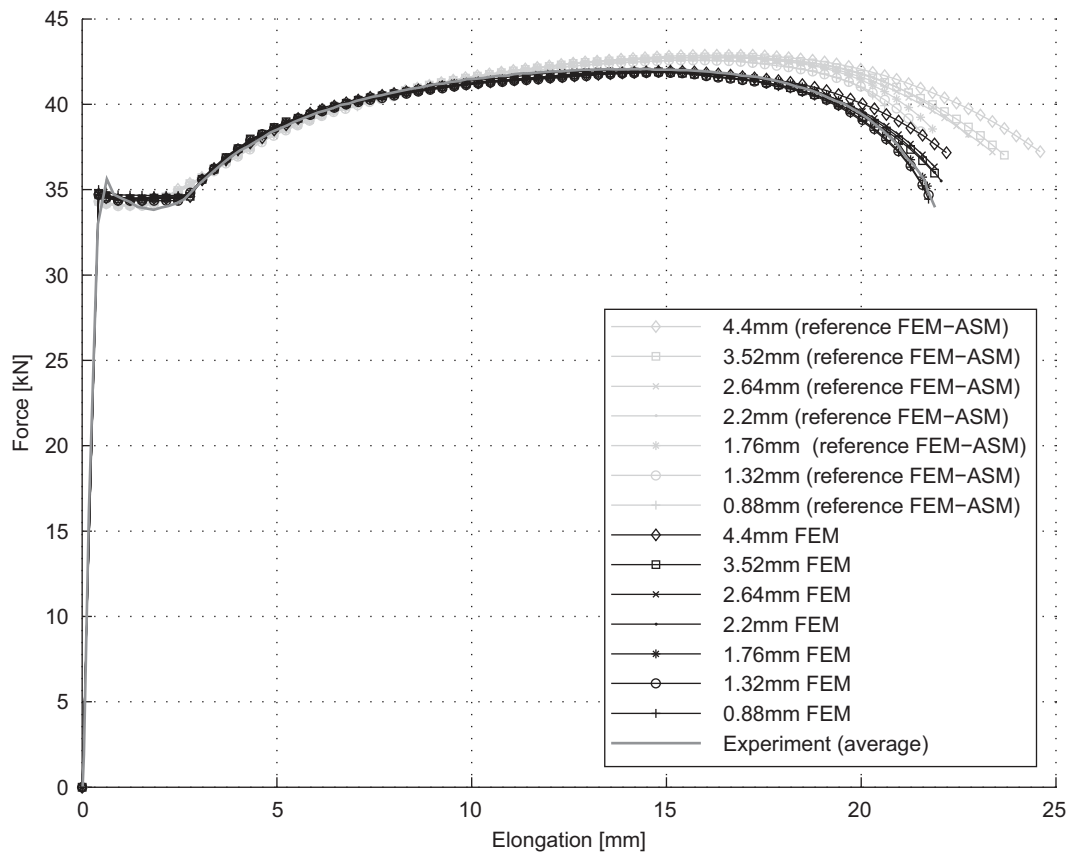

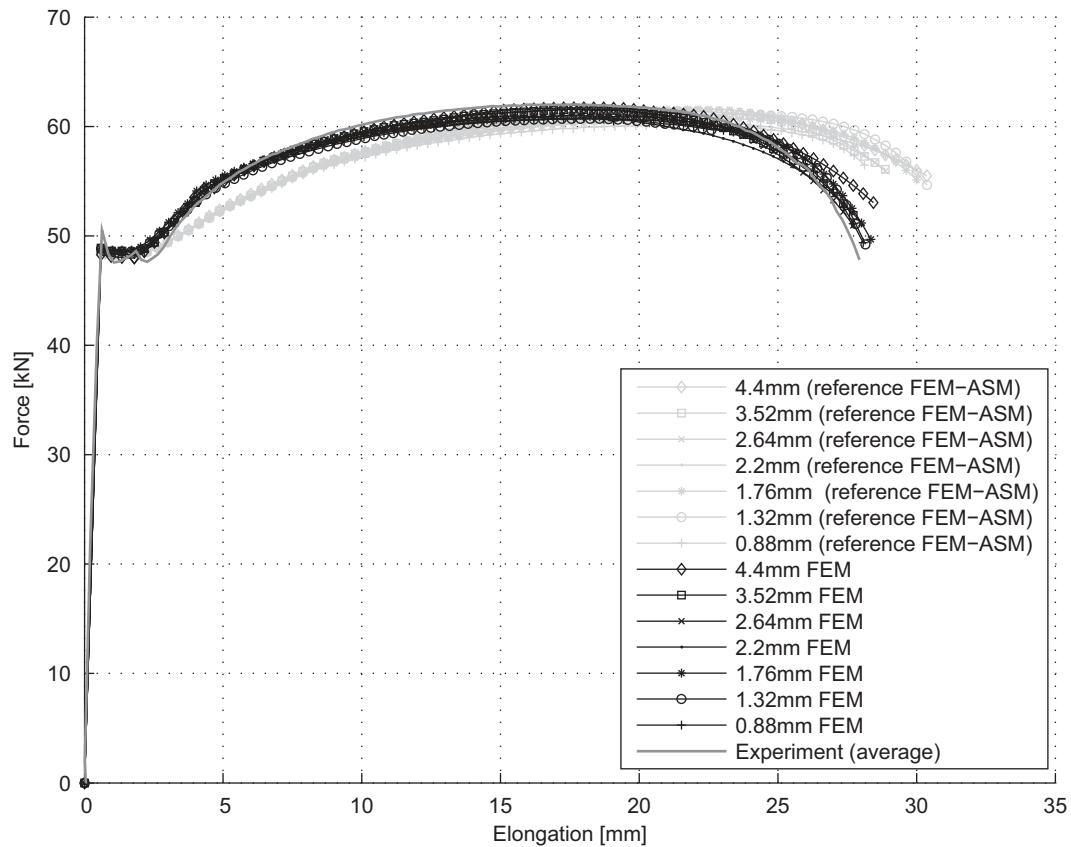**Fig. 14.** Finite element analysis results ($L/B = 8$).

Fig. 15. Finite element analysis results ($L/B = 8.5$).
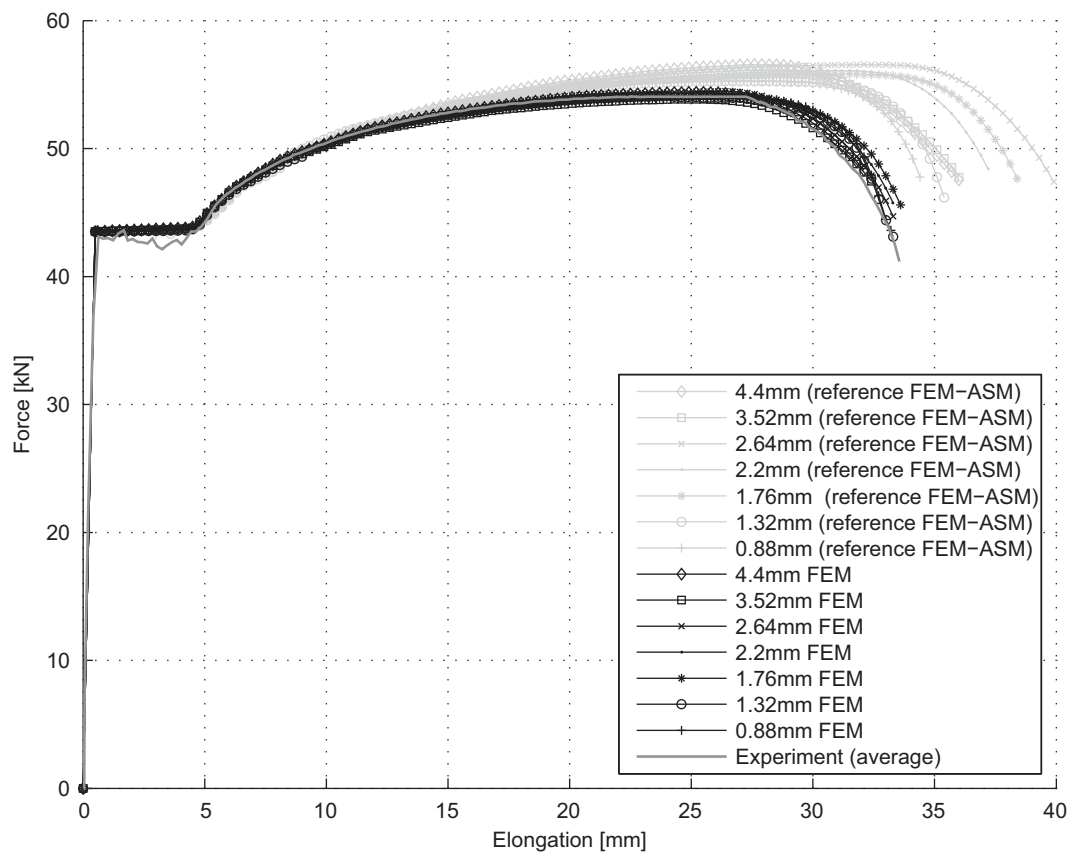

Fig. 16. Finite element analysis results ($L/B = 11.6$).

to the procedure presented in the ASM Handbook [22]. Their calculated force-elongation curve does not comply with the experiments as accurately as the proposed procedure. Furthermore, the point of failure is not predicted correctly, as the failure strain and the stress determination according to ASM is not finite element length dependent. This missing element length dependency of the power law fit results in a non-converging behaviour of the resulting force-elongation curves, whereas the proposed procedure results in a better convergence of results with varying element length.

5. Summary and conclusions

A procedure to obtain strain and stress until fracture suitable for finite element simulations using optical measurements is presented. The local strain is identified on the basis of the strain reference length. The stress is determined independently of the strain on the basis of the cross-sectional area of the specimen at any given instant as a function of the facet size. The decrease in cross-sectional area reduction with increasing facet size accounts for the averaging of the specimen's cross-section over the extent of the facet size and captures the overall physical behaviour. The finite element simulations are carried out with the finite element length equal to the strain reference lengths. These comparative finite element simulations show very good agreement with the independently recorded force-elongation curve from the MTS Test Frame. The proposed procedure predicts the point of failure sufficiently, whereas the presented ASM approach does not predict the point of failure precisely and does not show a converging behaviour for different element lengths. With increasing element lengths the proposed procedure predicts the point of failure slightly too early when compared to the experiments. The close ranges of triaxiality, Lode angle and parameter justify the choice of constant strain failure criteria. The triaxiality and Lode parameter are close to zero at the point of failure, see Fig. 6, as the specimens fail due to shear, see Bai and Wierzbicki [23]. The specimens encounter a compressive stress in breath and thickness direction in the necking region besides the longitudinal stress. This imposes that the assumption to obtain the true stress as a function of the specimen's cross-sectional area is not entirely correct after localization occurs. As a result the effective stress deviates in the necking region from the longitudinal stress, which is however used in the finite element simulations presented in this paper. Additionally, the shell element formulation does not consider stresses in thickness direction. Thereby only the stress over the specimen's breath is considered along with the stress in longitudinal specimen direction. However, the proposed procedure to obtain an element-length dependent strain and stress relation results in a significantly better force-elongation prediction until the point of failure for different mesh sizes than the conventional power law fit.

The future work will provide a correction of the strain and stress relation for shell elements within the localization region and the application and verification of the strain and stress relation for 3D structures.

Acknowledgment

Appendices A. Strain definition and extension of the 1D case

The 1D case needs to be extended to the 2D and 3D cases to quantitatively display the deformation of a surface element.

Therefore, the deformation gradient tensor **F** is introduced. **F** transforms a line element d**X** connecting the 3 facets in stage n into a line element d**x** in stage $n+1$, where in both cases the line element connects the same material coordinates

$$\delta \mathbf{x} = \mathbf{F}\, \delta \mathbf{X}. \tag{A.1}$$

Decomposition of Eq. (A.1) into a purely rotation matrix and pure stretch tensor gives

$$\mathbf{F} = \mathbf{R}\,\mathbf{U}, \tag{A.2}$$

where **R** describes the rotation of the points and the direction only. The coordinate-system dependent values for ε_x, ε_y, and ε_{xy} can be obtained directly from the symmetric stretch tensor **U** with the following form:

$$\mathbf{U} = \begin{pmatrix} 1 + \varepsilon_x & \varepsilon_{xy} \\ \varepsilon_{xy} & 1 + \varepsilon_y \end{pmatrix}. \tag{A.3}$$

To geometrically interpret the value of ε_{xy} GOM [24] defines a shear angle as follows:

$$\gamma_{xy} = \gamma_x + \gamma_y \text{ with}$$
$$\gamma_x = \arctan\left(\frac{\varepsilon_{xy}}{1 + \varepsilon_x}\right),$$
$$\gamma_y = \arctan\left(\frac{\varepsilon_{xy}}{1 + \varepsilon_y}\right). \tag{A.4}$$

Furthermore, the deformation gradient tensor **F** creates a functional connection of the coordinates of the deformed points $P_{v,i}$ with the coordinates of the undeformed points $P_{u,I}$

$$\mathbf{P}_{v,I} = \mathbf{u}_i + \mathbf{F}\mathbf{P}_{u,I}, \tag{A.5}$$

where $\mathbf{u}_i$ are the rigid body translations. The four unknown variables of Eq. (A.5) are the parameters of **F**. Hence, **F** can be calculated from a given 2D displacement field of points, where the undeformed and deformed states are known. A set of 3×3 neighbouring points is used to calculate **F**. Furthermore, the plane model of ARAMIS is used, assuming that a tangential plane (x'', y'') can approximate the local neighbourhood of a point; see Fig. A1.

To eliminate the coordinate dependency of the strain values, the calculation of the major and minor strain values is performed. From the main diagonal form of **U** the two eigenvalues λ_1 and λ_2 can be calculated from

$$\lambda_{1,2} = 1 + \frac{\varepsilon_x + \varepsilon_y}{2} \pm \sqrt{\left(\frac{\varepsilon_x + \varepsilon_y}{2}\right)^2 - (\varepsilon_x\,\varepsilon_y - \varepsilon_{xy}^2)}. \tag{A.6}$$

Substituting Eq. (A.6) into $\varepsilon_T = \ln(\lambda)$ returns the results in the appropriate strain measure, where the major strain follows the larger eigenvalue. Hence, the strain values are independent of the coordinate system.
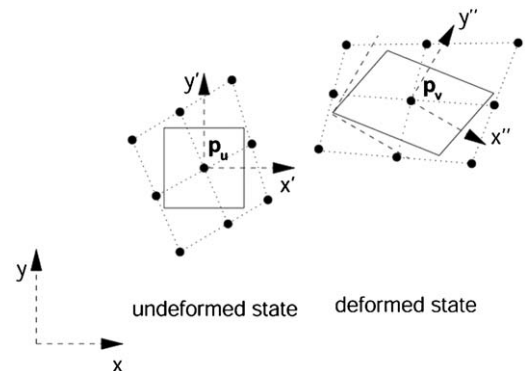

Fig. A1. A 3×3 neighbourhood for 2D strain calculation (ARAMIS [24]).
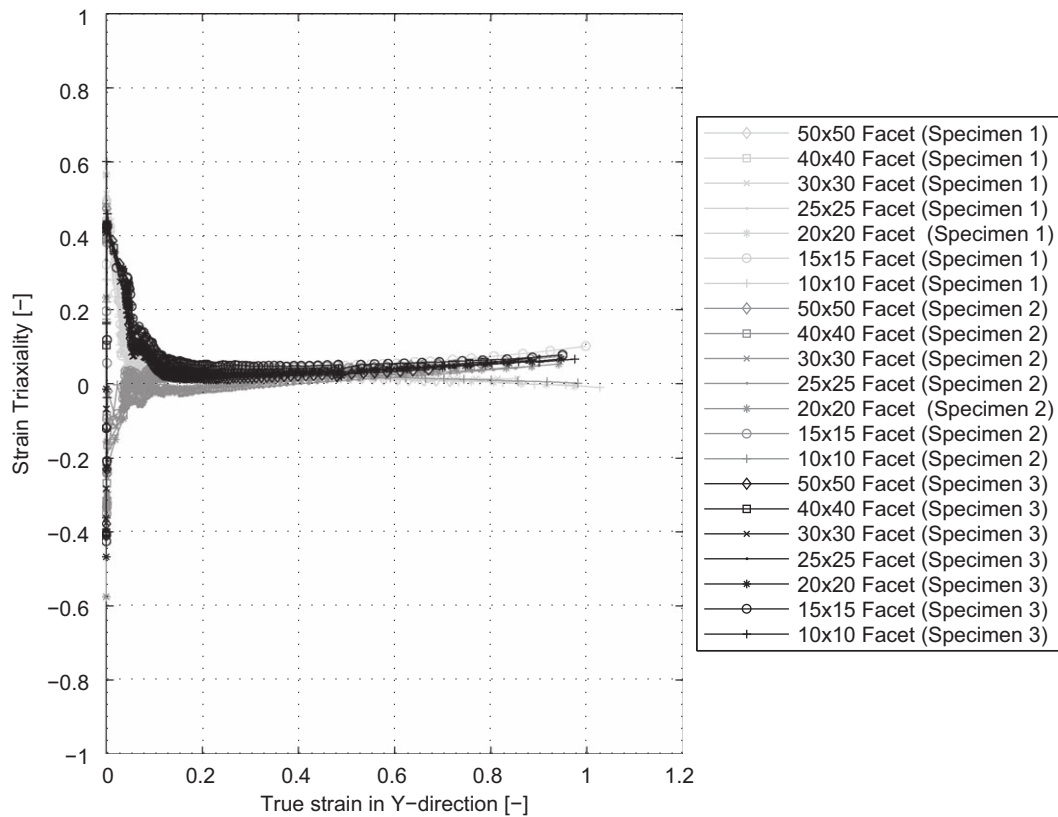
Fig. B1. Strain triaxiality versus true strain ($L/B = 8$).
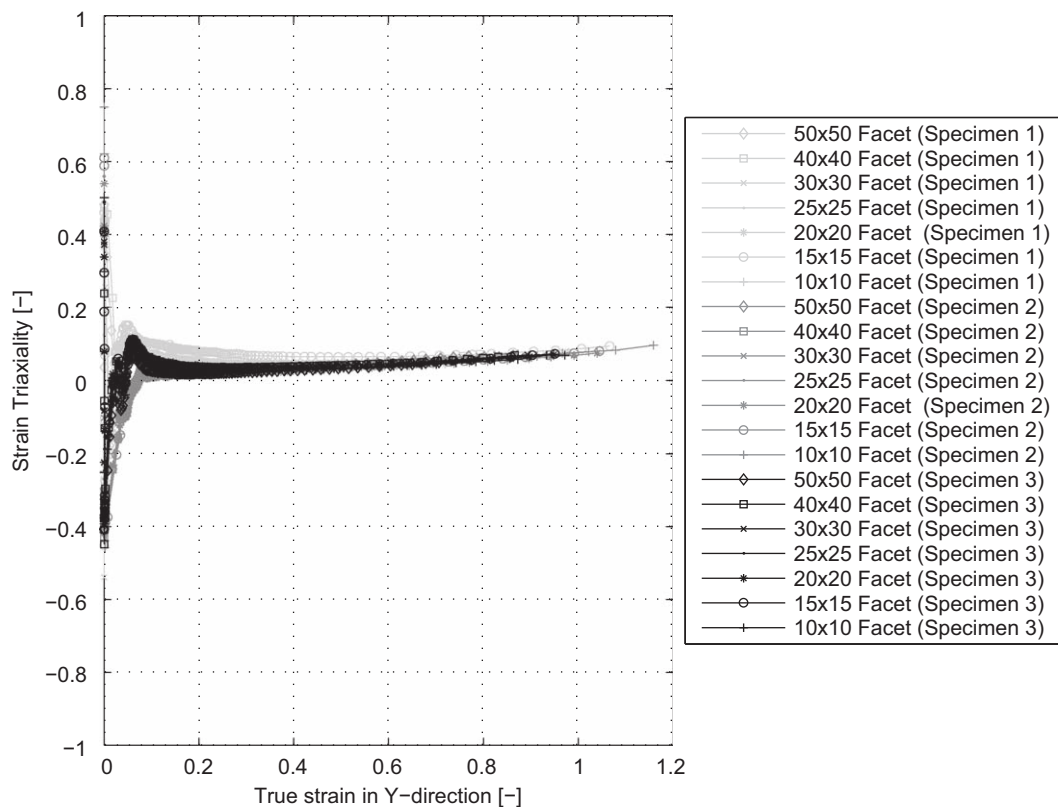

Fig. B2. Strain triaxiality versus true strain ($L/B = 8.5$).
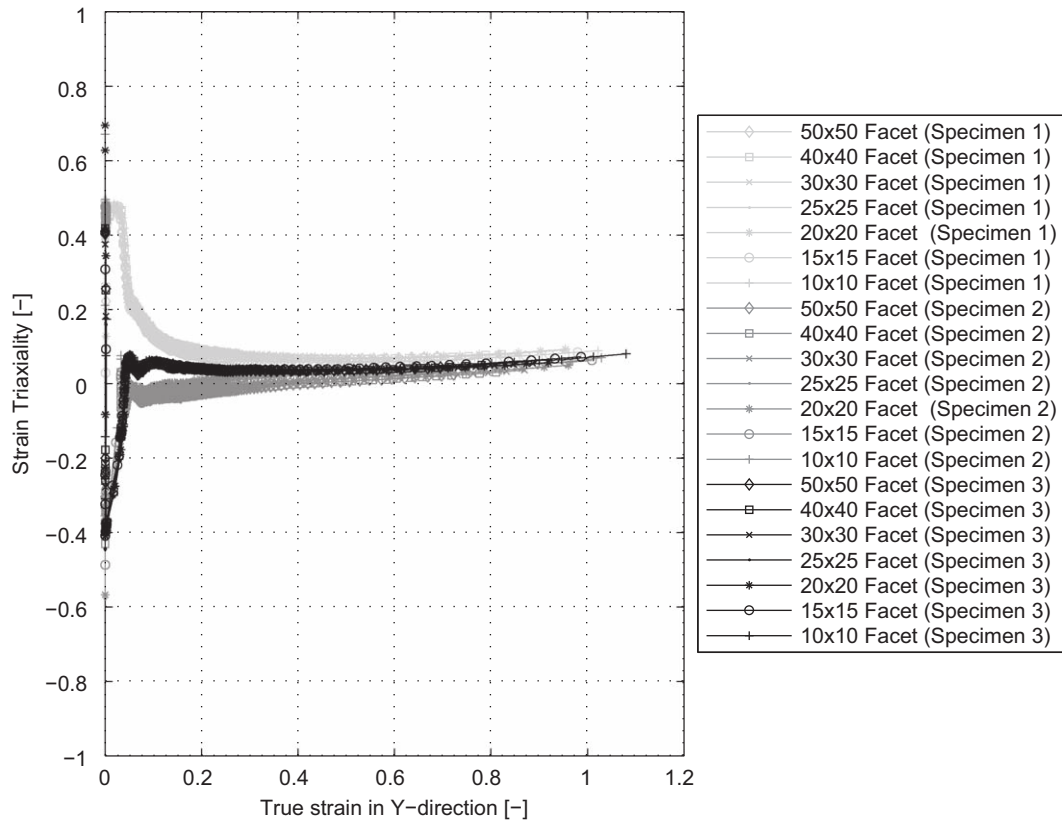
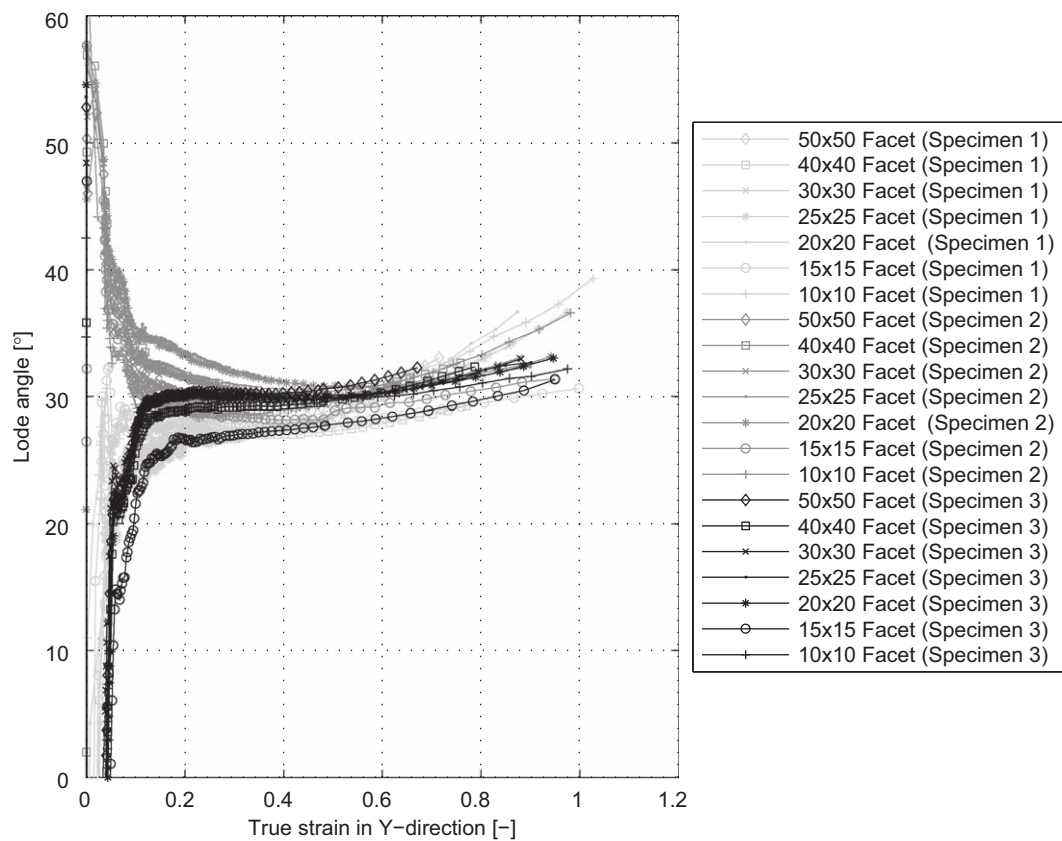**Fig. B3.** Strain triaxiality versus true strain ($L/B = 11.6$).

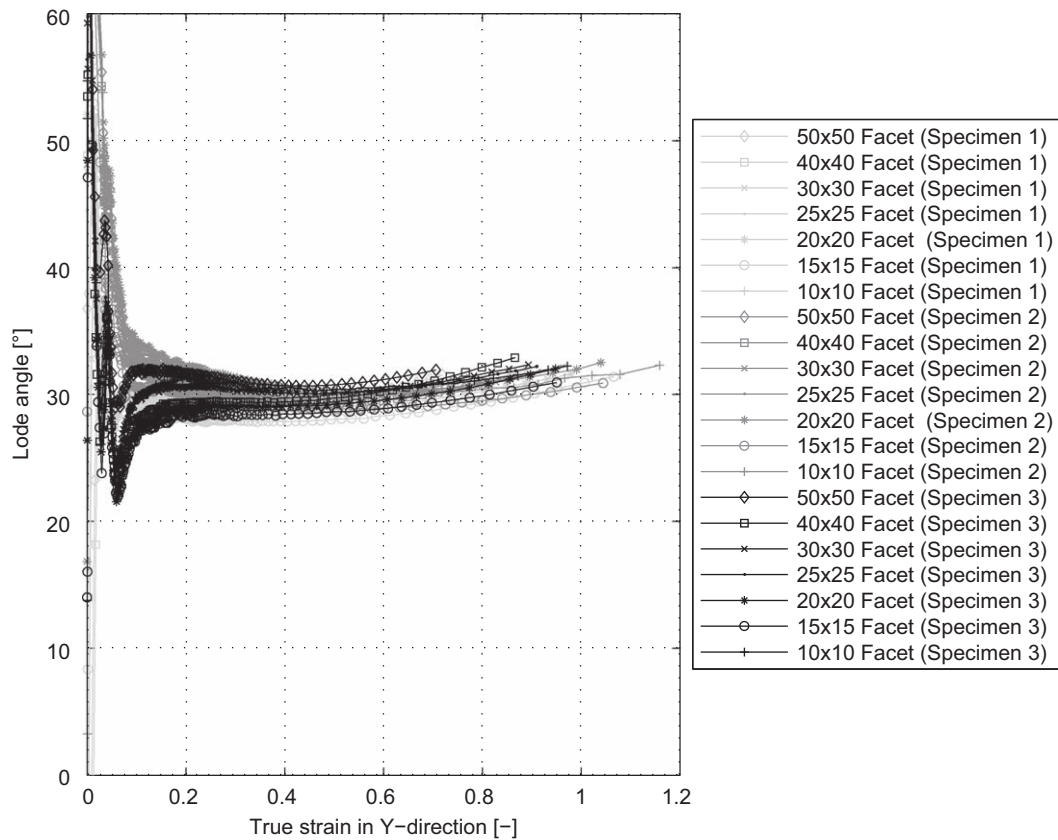**Fig. B4.** Lode angle versus true strain ($L/B = 8$).
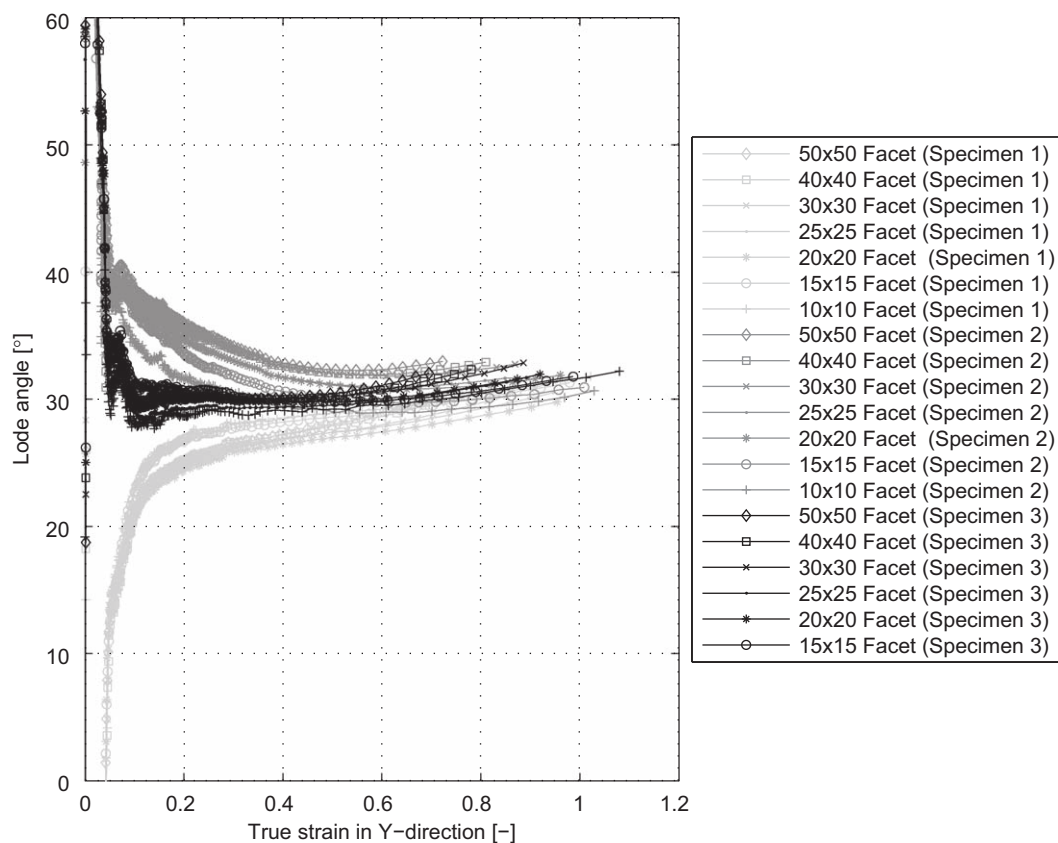
Fig. B5. Lode angle versus true strain ($L/B = 8.5$).
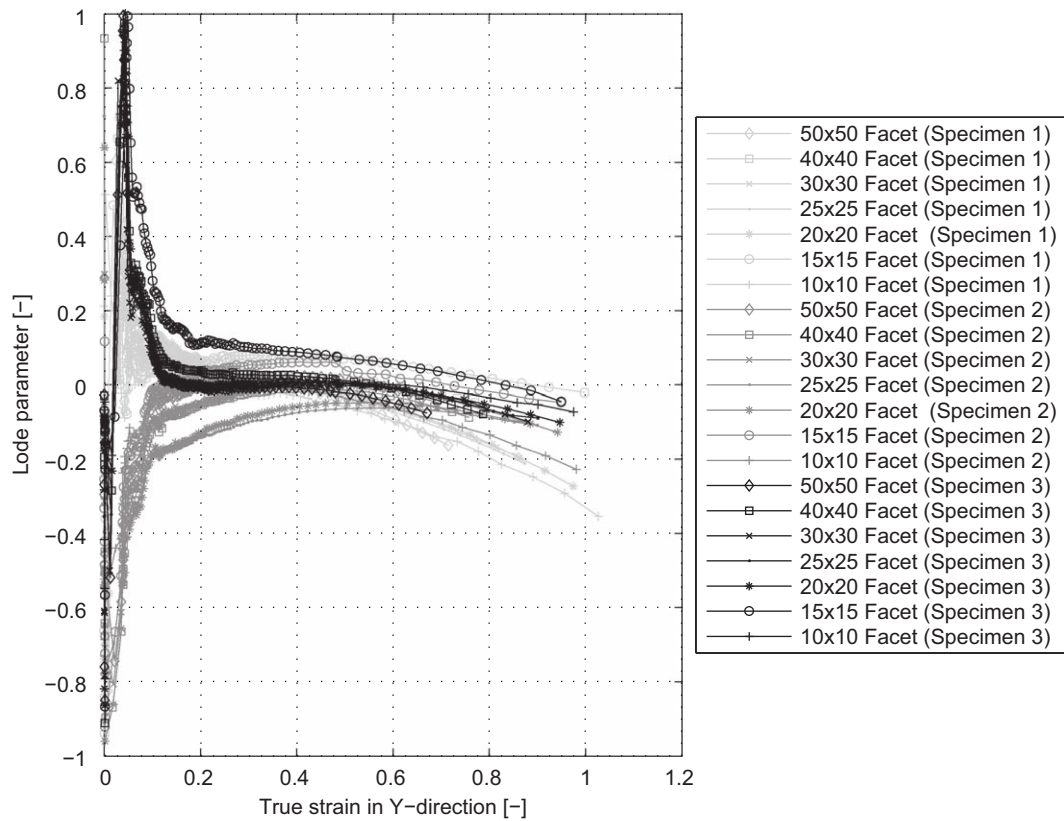

Fig. B6. Lode angle versus true strain ($L/B = 11.6$).

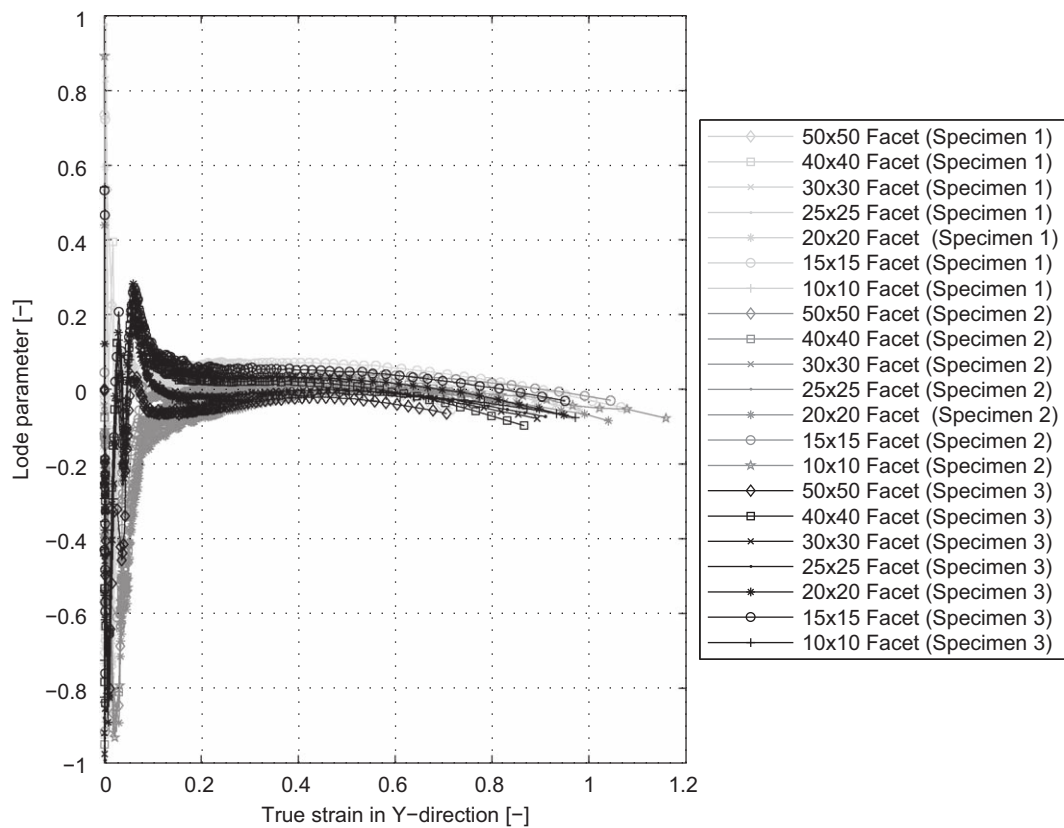**Fig. B7.** Lode parameter versus true strain ($L/B = 8$).

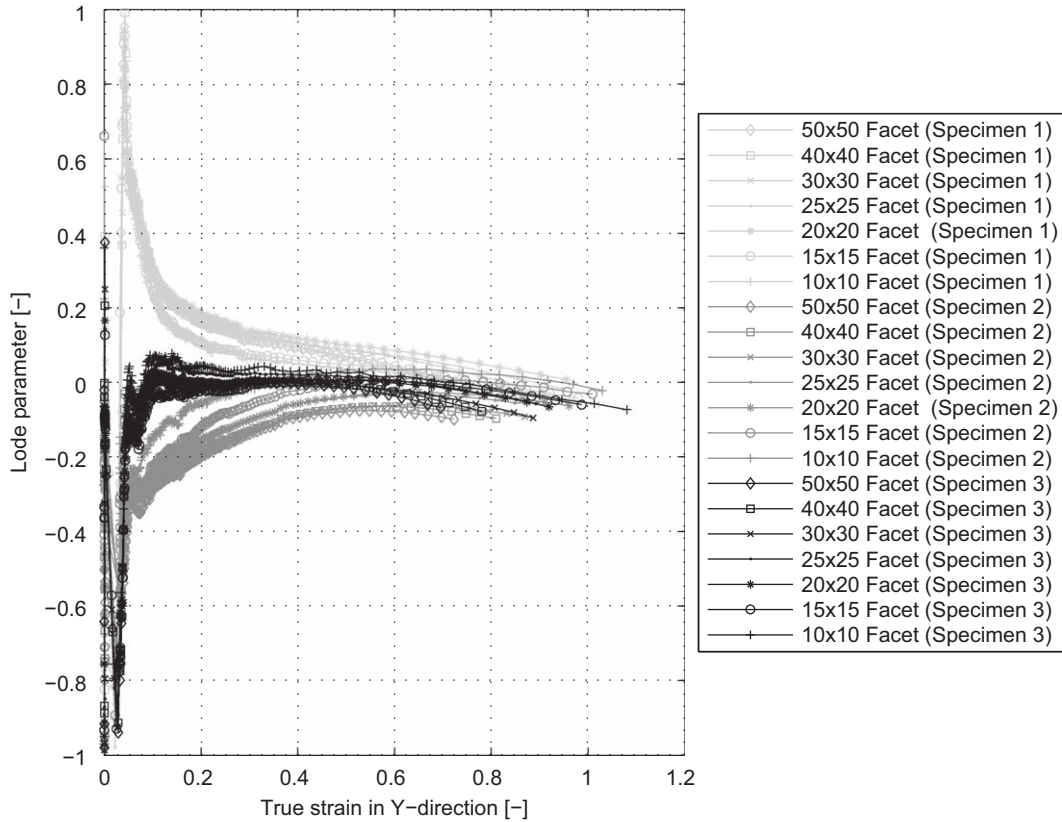**Fig. B8.** Lode parameter versus true strain ($L/B = 8.5$).

Fig. B9. Lode parameter versus true strain ($L/B = 11.6$).

Appendix B

Appendix B shows the strain triaxiality, Lode angel and parameter histories for all specimens and applied facet sizes, see Figs. B1–B9. The triaxiality is calculated based on the actual displacement measurements, respectively strain, according to

$$T = \frac{\varepsilon_{hyd}}{\varepsilon_m} = \frac{1/3\,(\varepsilon_x + \varepsilon_y + \varepsilon_z)}{\sqrt{2/3\,(\varepsilon_x^2 + \varepsilon_y^2 + \varepsilon_z^2)}}, \tag{B.1}$$

where ε_{hyd} is the hydrostatic strain and ε_m is the effective strain. The strain in thickness direction is calculated according to Eq. (1), where l is the initial thickness of the specimen, see Table 1, and δl is the thickness reduction, respectively out-of-plane displacement data, at the intersection of Sections 1 and 2. The Lode angle is calculated according to

$$\theta = \arctan \frac{2\varepsilon_z - \varepsilon_y - \varepsilon_x}{\sqrt{3}(\varepsilon_x - \varepsilon_y)}, \tag{B.2}$$

and the normalized Lode angle, see Bai and Wierzbicki [23], herein called Lode parameter, is calculated according to

$$\bar{\theta} = 1 - \frac{6\theta}{\pi}, \quad -1 \leqslant \bar{\theta} \leqslant 1. \tag{B.3}$$

References

[1] Joun MS, Eom JG, Lee MC. A new method for acquiring true stress-strain curves over a large range of strains using a tensile test and finite element method. Mechanics of Materials 2008;40:586–93.

[2] Koc P, Stok B. Computer-aided identification of the yield curve of a sheet metal after onset of necking. Computational Materials Science 2004;31(1–2):155–68.

[3] Mirone G. A new model for the elastoplastic characterization and the stress-strain determination on the necking section of a tensile specimen. International Journal of Solids and Structures 2004;41(13):3545–65.

[4] Paik JK. Practical techniques for finite element modelling to simulate structural crashworthiness in ship collision and grounding (Part I: Theory). Ships and Offshore Structures 2007;2(1):69–80.

[5] Springmann M, Kuna M. Identification of material parameters of the Gurson–Tvergaard–Needleman model by combined experimental and numerical techniques. Computational Materials Science 2005;32(3–4):544–52.

[6] Huatao J, Roehr U. Investigations of rupture failure of welding line. In: Proceedings of the 3rd International Conference on Collision and Grounding of Ships. Izu, Japan. 2004, p. 268–75.

[7] Isselin J, Lost A, Golel J, Najjar D, Bigerelle M. Assessment of the constitutive law by inverse methodology: small punch test and hardness. Journal of Nuclear Materials 2006;352(1–3):97–106.

[8] Zhang KS. Fracture prediction and necking analysis. Engineering Fracture Mechanics 1995;52(3):575–82.

[9] Zhang ZL, Hauge M, Ødegård J, Thaulow C. Determining material true stress-strain curve from tensile specimens with rectangular cross-section. International Journal of Solids and Structures 1999;36(23):3497–516.

[10] Bridgman PW. Studies in large flow and fracture. New York: McGraw-Hill; 1952.

[11] Ling Z. Uniaxial true stress-strain after necking. AMP Journal of Technology 1996;5:37–48.

[12] Hoffmann H, Vogl C. Determination of true stress-strain-curves and normal anisotropy tensile tests with optical strain measurement. CIRP Annals-Manufacturing Technology. 2003, vol. 52(1), p. 217–20.

[13] Ehlers S, Enquist B. Uniaxial tensile necking of steel dog-bone specimens. Helsinki University of Technology, Ship Laboratory. 2007, M-303.

[14] Remes H. Fatigue tests of CO_2-Laser, CO_2-Laser hybrid and submerged arc-welded butt joint of RAEX S275 LASER and NVA. Helsinki University of Technology, Ship Laboratory. 2003, M-278, 1, 7.

[15] Liu Y. Crashworthiness design of multi-corner thin-walled columns. Thin-Walled Structures 2008;46:1329–37.

[16] Zarei HR, Kröger M. Optimization of the foam-filled aluminum tubes for crush box application. Thin-Walled Structures 2008;46:214–21.

[17] Ehlers S, Tabri K, Schillo N, Ranta J. Implementation of a novel ship side structure into a tanker and a ropax vessel for increased crashworthiness. 6th European LS-DYNA Users' Conference, Gothenburg, Sweden. 2007, 4.111–4.120.

[18] Harewood FJ, McHugh PE. Comparison of the implicit and explicit finite element methods using crystal plasticity. Computational Materials Science 2007;39:481–94.

[19] Ehlers S, Broekhuijsen J, Alsos HS, Biehl F, Tabri K. Simulating the collision response of ship side structures; a failure criteria benchmark study. International Shipbuilding Progress 2008;55:127–44.

[20] Hallquist JO. LS-DYNA Theory Manual. Livermore Software Technology Corporation. 2005.

[21] Tabri K, Alsos H, Broekhuijsen J, Ehlers S. A benchmark study on ductile failure criteria for shell elements in multiaxial stress state. In: Proceedings of Marstruct, Glasgow, United Kingdom. 2007, p. 401–9.

[22] ASM handbook. Mechanical Testing and Evaluation. 2000, vol. 8.

[23] Bai Y, Wierzbicki T. A new model of metal plasticity and fracture with pressure and Lode dependence. International Journal of Plasticity 2008;24:1071–96.

[24] ARAMIS user manual—Software v6, 25.4.2007, Gesellschaft für Optische Messtechnik.